Check for updates

Enhanced hydrogen storage kinetics and air stability of nanoconfined NaAlH₄ in graphene oxide framework†

Hyung Wan Do,‡ HyeonJi Kim and Eun Seon Cho [ID] *

With a growing concern over climate change, hydrogen offers a wide range of opportunities for decarbonization and provides a flexibility in overall energy systems. While hydrogen energy is already plugged into industrial sectors, a physical hydrogen storage system poses a formidable challenge, giving momentum for safe and efficient solid-state hydrogen storage. Accommodating such demands, sodium alanate (NaAlH₄) has been considered one of the candidate materials due to its high storage capacity. However, it requires a high temperature for hydrogen desorption and becomes inactive irreversibly upon air-exposure. To enhance sluggish reaction kinetics and reduce the hydrogen desorption temperature, NaAlH₄ can be confined into a porous nanoscaffold; however, nanoconfined NaAlH₄ with sufficient hydrogen storage performance and competent stability has not been demonstrated so far. In this work, we demonstrate a simultaneously enhanced hydrogen storage performance and air-stability for NaAlH₄ particles confined in a nanoporous graphene oxide framework (GOF). The structure of the GOF was elaborately optimized as a nanoscaffold, and NaAlH₄ was infiltrated into the pores of the GOF *via* incipient wetness impregnation. As a result of the nanoconfinement, both the onset temperature and activation energy for hydrogen desorption of NaAlH₄ are significantly decreased without transition metal catalysts, while simultaneously achieving the stability under ambient conditions.

Introduction

Hydrogen has emerged as a clean and sustainable energy source capable of fulfilling growing global energy demand and potentially substituting traditional fossil fuels.[1] Metal hydrides are suitable candidates for safe and high-density solid-state hydrogen storage, although several challenges in kinetic and thermodynamic requirements must still be overcome.[2] Among metal hydrides, sodium alanate (NaAlH₄) has been widely investigated owing to its high hydrogen storage capacity (7.4 wt%) and moderate decomposition temperature (~180 °C).[3] However, its slow hydrogen desorption kinetics and limited reversibility must be addressed for practical applications, along with a stability issue under ambient conditions in which NaAlH₄ tends to lose its hydrogen storage capability similar to other metal hydrides. To overcome these issues, a variety of Ti- and Ce-based catalytic additives have been used to improve the hydrogen storage performance of NaAlH₄.[4–8] Rapid hydrogen

desorption at temperatures below 100 °C and superior cycling properties have been demonstrated using high-performance transition metal–carbon composite catalysts.[9,10] In addition to such transition metal-based catalysts, nanoconfinement of metal hydrides into a variety of nanoporous scaffolds has been employed. By effectively confining the metal hydrides inside nanopores of the scaffold, it is possible to achieve nanoparticles with dimensions below 10 nm.[11,12] Nanoconfinement shortens the diffusion length of hydrogen atoms while increasing the number of grain boundaries and surface area, thereby improving hydrogen storage performance of metal hydrides. A wide range of host materials for NaAlH₄ have been previously demonstrated, including mesoporous carbon,[13–15] carbon aerogel,[16] carbon nanofiber,[17,18] carbon nanotube,[19] mesoporous silica,[20] metal–organic framework,[21,22] and porous aluminium scaffold.[23] Most of the prior works have focused on enhancing reaction kinetics and reversibility, and to our knowledge there have been no studies on increasing air stability of the nanoconfined NaAlH₄.

Here, we report a nanocomposite of NaAlH₄ confined into graphene oxide framework (NaAlH₄@GOF) *via* incipient wetness impregnation, and discuss its enhanced hydrogen desorption kinetics as well as air stability compared to those of bulk NaAlH₄. A GOF is an expansion of GO layers by pillar molecules, and it has been shown as a promising material for gas storage,[24] nanofiltration membrane,[25] and ion-selective

Department of Chemical and Biomolecular Engineering, Korea Advanced Institute of Science and Technology (KAIST), Daejeon 34141, Republic of Korea. E-mail: escho@kaist.ac.kr

‡ Current address: KIURI Institute, Yonsei University, Seoul 03722, Republic of Korea.

protective layer for redox-flow batteries[26] because of a high surface area and adjustable interlayer spacing, simultaneously taking advantage of robustness and chemical versatility of GO. By virtue of such characteristics, GOF with a three-dimensional framework structure is an ideal host material for complex metal hydrides. Also, a gas-selective property of GO layers is expected to function as a protective layer for the confined metal hydrides.[27]

Experimental

Synthesis of graphene oxide framework (GOF)

To synthesize GOF, 200 mg of graphene oxide powder (Grapheneall Co., Ltd) was first dispersed in 20 mL of methanol *via* sonication at room temperature for 1 h. The dispersion was then transferred into a Teflon-lined autoclave, and 400 mg of benzene-1,4-diboronic acid (B14DBA, Alfa Aesar, 96% purity) was added to the dispersion. The solvothermal reaction was performed at 100 °C for 48 h in an autoclave reactor. After cooling down to room temperature, the mixture was centrifuged at 10 000 rpm for 20 min and washed with methanol three times to remove the unreacted excess B14DBA linker molecules. The resulting GOF was dried under vacuum at 120 °C for 24 h and stored inside an Ar-filled glovebox for the subsequent $NaAlH_4$ infiltration process.

Synthesis of $NaAlH_4$ impregnated GOF ($NaAlH_4$@GOF)

The infiltration of $NaAlH_4$ into the GOF was performed under an Ar atmosphere. $NaAlH_4$ was purified by dissolving the as-purchased $NaAlH_4$ (Sigma-Aldrich, 93% purity, hydrogen storage grade) in anhydrous tetrahydrofuran (THF) and removing metallic impurities using a PTFE syringe filter (CHMLAB Group) with a pore size of 0.2 μm. The 1 M solution of $NaAlH_4$ in THF was prepared using the purified $NaAlH_4$. The 50–100 mg of GOF was added to 10 mL of the $NaAlH_4$ solution, and the mixture was magnetically stirred at room temperature for 15 h. To collect $NaAlH_4$ impregnated GOF composite, the mixture was centrifuged at 10 000 rpm for 20 min and washed with THF three times to remove bulk $NaAlH_4$ that may have been recrystallized on the surface of the GOF. The resulting $NaAlH_4$@GOF composite was vacuum-dried at room temperature overnight and stored in an Ar-filled glovebox until further analysis.

Material characterization

X-ray diffraction patterns for measuring interlayer spacing were acquired with a Rigaku SmartLab. N_2 adsorption–desorption isotherms for specific surface area and pore size distribution were obtained with a Micromeritics 3Flex. Fourier-transform infrared spectroscopy (Bruker, Alpha), thermogravimetric analysis (Netzsch, TG 209 F1 Libra), and X-ray photoelectron spectroscopy (Thermo Scientific, K-Alpha) measurements were also performed to verify successful synthesis and characterize properties of the synthesized products. The $NaAlH_4$ mass loading inside $NaAlH_4$@GOF composite was measured *via*

inductively coupled plasma-optical emission spectroscopy (Agilent, 720 ICP-OES).

Measurement of hydrogen desorption performance

The hydrogen desorption performance of bulk $NaAlH_4$ and $NaAlH_4$@GOF was measured by temperature programmed desorption mass spectrometry (TPD-MS) using a MicrotracBEL BELCAT II catalyst analyser and BELMass quadrupole mass spectrometer. Calibration was performed prior to the measurements using a mixture gas of H_2 and Ar with a known H_2 concentration. The 50–100 mg of $NaAlH_4$@GOF composite was loaded into a quartz sample holder and purged with Ar for 30 min. The sample was ramped from room temperature to 500 °C with a heating rate of 2.5–20.0 °C min^{-1} under a constant flow (30 mL min^{-1}) of Ar carrier gas, and the final temperature was held at 500 °C for 30 min to ensure a complete desorption.

Results and discussion

Synthesis and optimization of GOF

GOF was synthesized *via* solvothermal reaction of graphene oxide (GO) with benzene-1,4-diboronic acid (B14DBA) in methanol,[24] as shown in Fig. 1a. B14DBA was chosen as the linker material based on good reactivity of boronic acids with hydroxyl functional groups of GO,[28] and relatively short length of the B14DBA molecule which is composed of a single phenyl ring unit connected to the boronic acids. Alternative choice of linkers may be considered to readily modify a physical property of the resulting GOF as necessary. For example, *d*-spacing of the GOF can be slightly increased by using a linker with a longer length (*e.g.* 4,4'-biphenyldiboronic acid).[29] To optimize physical properties of the framework before $NaAlH_4$ infiltration, we synthesized a series of GOFs by varying the ratio of GO and B14DBA – referred as GOF (1 : *x*) where *x* is the ratio of B14DBA relative to GO. Changes in *d*-spacing and Brunauer–Emmett–Teller (BET) specific surface area were measured *via* X-ray diffraction (XRD) and N_2 adsorption–desorption isotherm experiments, respectively, to confirm successful synthesis of a three-dimensional nanoporous framework structure. Fig. 1b and S1a† show a monotonic increase in the *d*-spacing of GOF with increasing linker concentration. As more linker molecules are intercalated into the GO structures, the overall alignment angle between the linker and GO moves closer to being perpendicular and the diffraction peak shifts to a lower angle. The corresponding interlayer distance between the GO sheets is expanded from 0.86 nm to 1.06 nm, reaching a maximum value beyond GO to B14DBA ratio of 1 : 2. Furthermore, the XRD patterns with a single diffraction peak indicate a well-defined layer structure for the GOF as well as full removal of unreacted linkers. Fig. 1c and S1b† show type I (microporous) isotherms with a maximum BET specific surface area of 200.5 $m^2 g^{-1}$ for GO to B14DBA ratio of 1 : 2, comparable to previously reported values[24,29] and much higher than 4.6 $m^2 g^{-1}$ for as-received GO. Average pore diameter is calculated to be around 2 nm (Fig. S2†), confirming a nanoporous structure. Once the maximum BET specific surface area is reached for GOF (1 : 2),
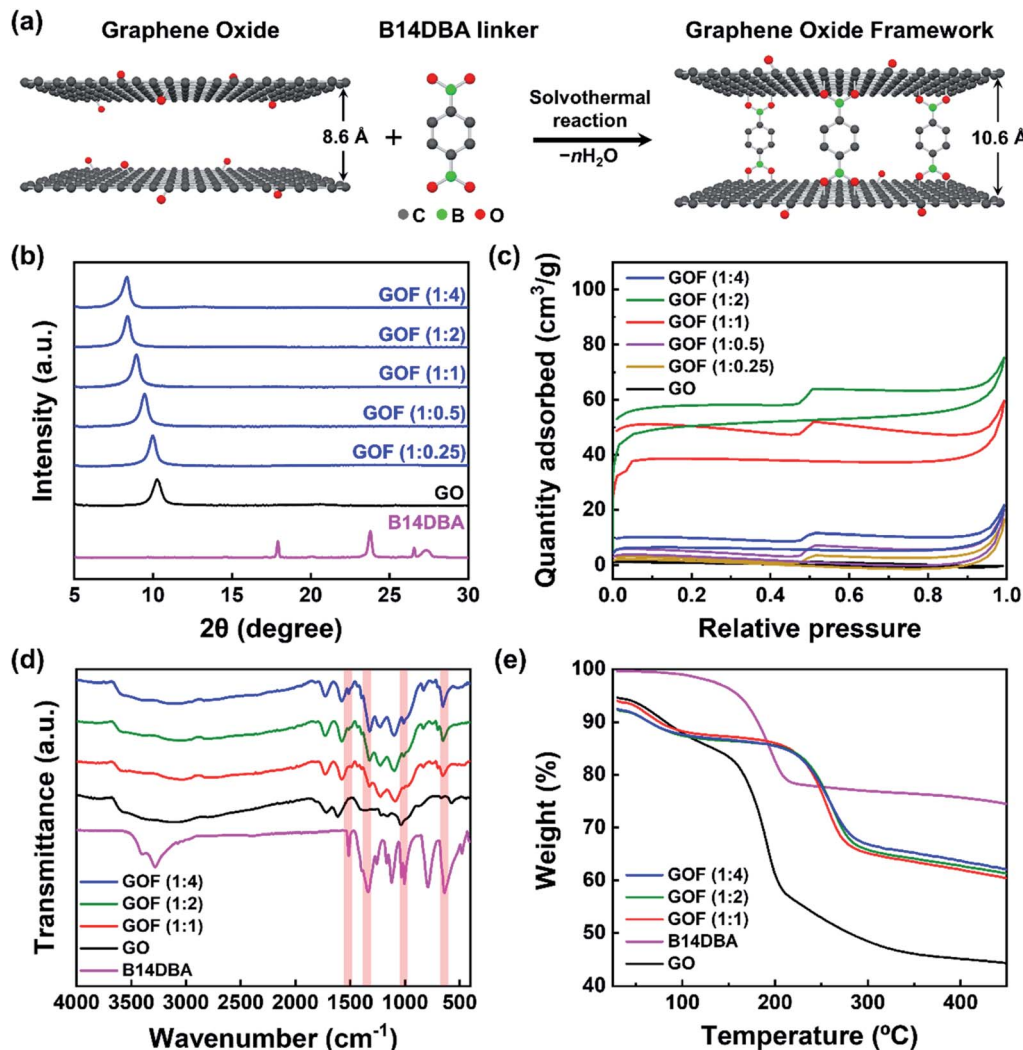
Fig. 1 Synthesis and characterization of GOF. (a) A schematic diagram illustrating solvothermal reaction of GO and B14DBA linker to produce GOF. (b) XRD patterns of B14DBA, GO, and GOF synthesized using different ratios of GO and B14DBA. (c) N_2 adsorption–desorption isotherms of GO and synthesized GOFs. (d) FT-IR spectra of B14DBA, GO, and synthesized GOFs. Characteristic bands of B14DBA are indicated in red. (e) TGA curves of GO, B14DBA, and synthesized GOFs.

an additional increase in the linker concentration leads to a decrease in the BET specific surface area with negligible increase in the d-spacing. Based on these results, we chose GOF (1 : 2) as the optimal scaffold for $NaAlH_4$ impregnation.

To further verify the formation of chemical bonding between GO and B14DBA, Fourier transform infrared spectroscopy (FT-IR) and thermogravimetric analysis (TGA) were performed. The FT-IR spectra (Fig. 1d) of GOF (1 : 1), GOF (1 : 2), and GOF (1 : 4) exhibit characteristic B–O deformation at ≈ 680 cm^{-1}, B–C vibration at ≈ 1080 cm^{-1}, B–O stretch at ≈ 1340 cm^{-1}, and C=C stretch at ≈ 1520 cm^{-1},[29] which are clearly observed in B14DBA but not in GO. A broad O–H stretch around 3200 cm^{-1} is also observed, indicating that some functional groups of GO remain in GOF after the solvothermal process. Moreover, the TGA curves (Fig. 1e) of GOF show a rapid mass loss around 220 °C due to decomposition of oxygen-containing functional groups,[29] compared to a lower decomposition temperature

around 150 °C for both GO and B14DBA. Combined with the increased d-spacing, enhanced BET specific surface area, and FT-IR measurements, this improved thermal stability suggests that B14DBA forms new chemical bonds with GO to evolve into a nanoporous framework, rather than simply being intercalated between the GO sheets.

Preparation of $NaAlH_4$@GOF nanocomposites

$NaAlH_4$ was infiltrated into the nanoporous GOF *via* incipient wetness impregnation using solutions of purified $NaAlH_4$ in tetrahydrofuran (THF), as illustrated in Fig. 2a. Wetness impregnation was chosen over melt infiltration as the method for preparing $NaAlH_4$@GOF based on the thermal stability of GOF as well as the simplicity and low cost of the solution-based synthesis process. We used three different $NaAlH_4$ concentrations (0.25 M, 1 M, and 3 M) for the impregnation process to determine the optimal process condition. The resulting $NaAlH_4$
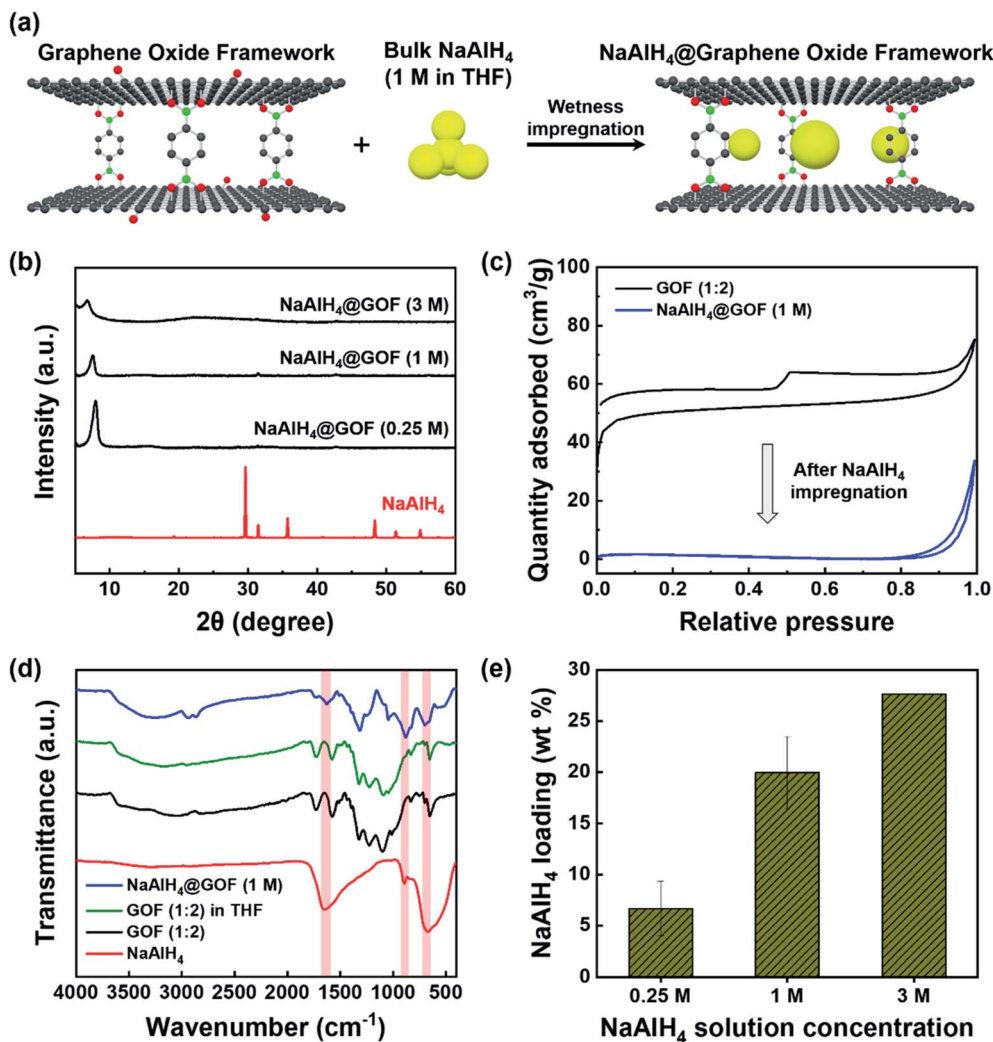
Fig. 2 Synthesis and characterization of NaAlH$_4$@GOF. (a) Schematic diagram illustrating incipient wetness impregnation of NaAlH$_4$ into nanopores of GOF. (b) XRD patterns of as-received NaAlH$_4$ and NaAlH$_4$@GOF prepared using solutions with different NaAlH$_4$ concentrations. (c) N$_2$ adsorption–desorption isotherms of GOF (1 : 2) and NaAlH$_4$@GOF (1 M). A significant decrease in BET specific surface area was observed upon NaAlH$_4$ infiltration. (d) FT-IR spectra of NaAlH$_4$, as-synthesized GOF (1 : 2), GOF (1 : 2) treated with THF for 15 h, and synthesized NaAlH$_4$@GOF (1 M). Characteristic bands of NaAlH$_4$ are indicated in red. (e) NaAlH$_4$ loading inside NaAlH$_4$@GOFs prepared using NaAlH$_4$ solutions of various concentrations, obtained from ICP-OES analysis.

infiltrated GOFs were referred to as NaAlH$_4$@GOF (x M) where x is the concentration of NaAlH$_4$ in THF.

As shown in the XRD patterns of bulk NaAlH$_4$ and NaAlH$_4$@GOFs (Fig. 2b), the sharp diffraction peaks from crystalline NaAlH$_4$ are not observed for NaAlH$_4$@GOFs. This implies a successful confinement of NaAlH$_4$ inside the nanoporous scaffold resulting in nanocrystalline NaAlH$_4$ and causing severe peak broadening, since amorphous NaAlH$_4$ bulk phase has never been observed in NaAlH$_4$ infiltrated nanoporous composites.[22] Furthermore, a complete removal of recrystallized NaAlH$_4$ that may have formed on the surface of the GOF is also verified from the XRD results. When a solution with a higher NaAlH$_4$ concentration was used for wetness impregnation, the diffraction peak of NaAlH$_4$@GOF is broadened and the d-spacing increases from 1.10 nm (0.25 M) and 1.17 nm (1 M) to 1.28 nm (3 M), suggesting that an extreme

NaAlH$_4$ loading may have a detrimental effect on the structural integrity of the framework (Fig. S3†). The surface morphology of GOF and NaAlH$_4$@GOF from transmission electron microscopy (TEM) images do not show any significant differences upon NaAlH$_4$ infiltration (Fig. S4†). In bright field scanning transmission electron microscopy with energy-dispersive X-ray spectroscopy (BF-STEM-EDS) measurements, the images of NaAlH$_4$@GOF indicate the coexistence of GOF and confined NaAlH$_4$; Na and Al mapping originated from NaAlH$_4$ coincide with carbon and oxygen from GOF, which presents a successful confinement of NaAlH$_4$ into GOF (Fig. S5†).

We additionally confirmed a successful infiltration of NaAlH$_4$ inside the GOF through N$_2$ adsorption–desorption isotherm and FT-IR measurements. Subsequent to the impregnation process, BET specific surface area of NaAlH$_4$@-GOF (1 M) is reduced to 6.6 m^2 g^{-1}, compared to 200.5 m^2 g^{-1}

for as-synthesized GOF (Fig. 2c). The FT-IR spectra of NaAlH$_4$@GOF (1 M) shown in Fig. 2d clearly display Al–H bending modes at $\approx$670 cm^{-1} and 890 cm^{-1}, and Al–H stretching modes at $\approx$1650 cm^{-1},[30] which are not observed in GOF. A FT-IR spectrum of GOF treated with THF for 15 h without NaAlH$_4$ was also measured as a control, which shows no change compared to before the THF treatment. Finally, NaAlH$_4$ mass loading inside the NaAlH$_4$@GOF composite was calculated for each NaAlH$_4$ solution concentration (Fig. 2e) using Al content determined from inductively coupled plasma-optical emission spectroscopy (ICP-OES) measurements. The resulting NaAlH$_4$ loadings were 6.7 wt% for NaAlH$_4$@GOF (0.25 M), 20.0 wt% for NaAlH$_4$@GOF (1 M), and 27.6 wt% for NaAlH$_4$@GOF (3 M), demonstrating a comparable or higher mass loading of active materials relative to other existing porous scaffolds.[12]

Hydrogen desorption performance and air-stability of NaAlH$_4$@GOF

The hydrogen desorption reaction of NaAlH$_4$ consists of three steps, as shown in Fig. 3a. Hydrogen desorption properties of NaAlH$_4$@GOF (1 M) were measured using temperature programmed desorption mass spectrometry (TPD-MS) and compared with those of bulk NaAlH$_4$. The TPD-MS profiles at different heating rates and the corresponding Kissinger plots for bulk NaAlH$_4$ and NaAlH$_4$@GOF (1 M) are shown in Fig. 3b–e. The TPD-MS curves of bulk NaAlH$_4$ (Fig. 3b) present an onset desorption temperature at 180 °C, close to the melting point of NaAlH$_4$. However, NaAlH$_4$@GOF (1 M) starts to release hydrogen at room temperature, in agreement with the previous reports that hydrogen desorption starts at ambient temperature for nanoconfined NaAlH$_4$ with particle size below 10 nm.[18,19,31]
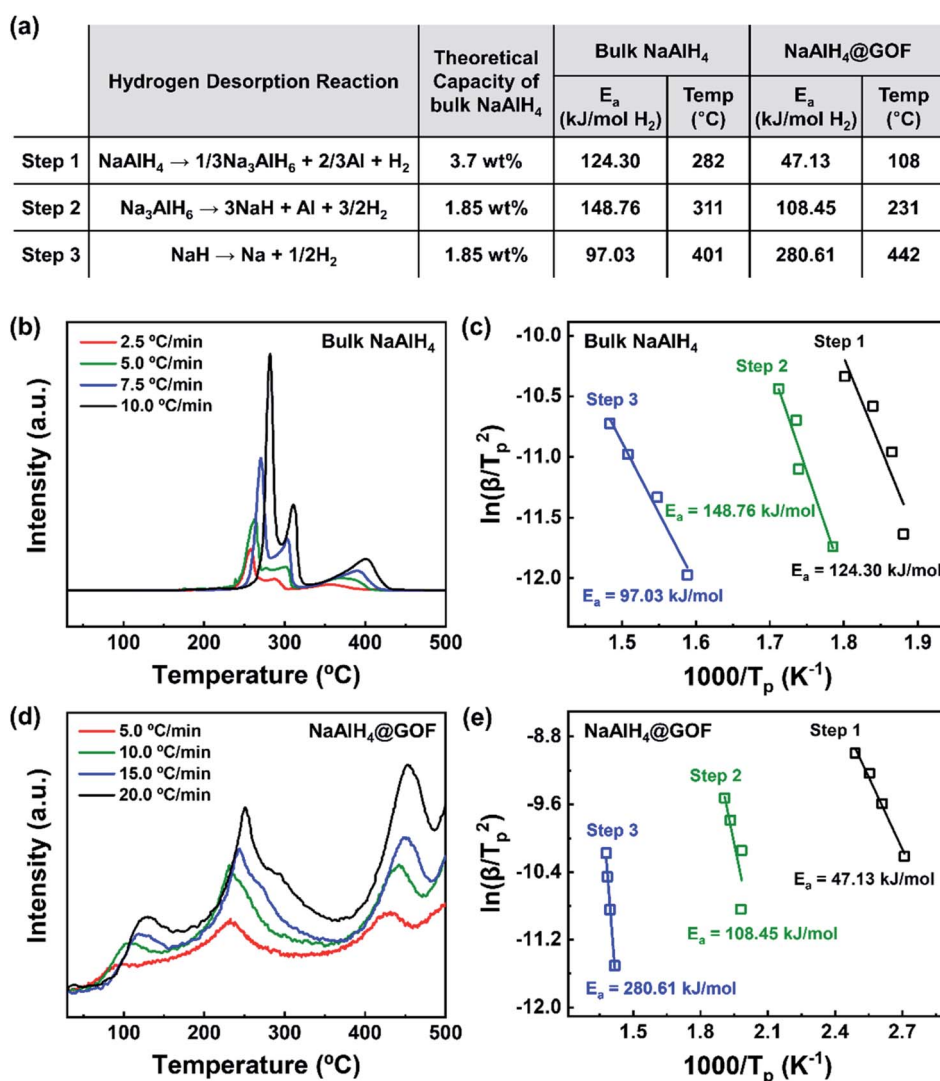

Fig. 3 Hydrogen desorption performance of bulk NaAlH$_4$ and NaAlH$_4$@GOF (1 M). (a) Hydrogen desorption mechanism and corresponding theoretical capacity of bulk NaAlH$_4$, along with activation energy and peak desorption temperature at a heating rate of 10.0 °C min^{-1} for bulk NaAlH$_4$ and NaAlH$_4$@GOF. (b) TPD-MS profiles of bulk NaAlH$_4$ at heating rates of 2.5 °C min^{-1}, 5.0 °C min^{-1}, 7.5 °C min^{-1}, and 10.0 °C min^{-1}. (c) Kissinger plots with corresponding E_a for the three hydrogen desorption reactions of bulk NaAlH$_4$. (d) TPD-MS profiles of NaAlH$_4$@GOF (1 M) at heating rates of 5.0 °C min^{-1}, 10.0 °C min^{-1}, 15.0 °C min^{-1}, and 20.0 °C min^{-1}. (e) Kissinger plots with corresponding E_a for the three hydrogen desorption reactions of NaAlH$_4$@GOF (1 M).
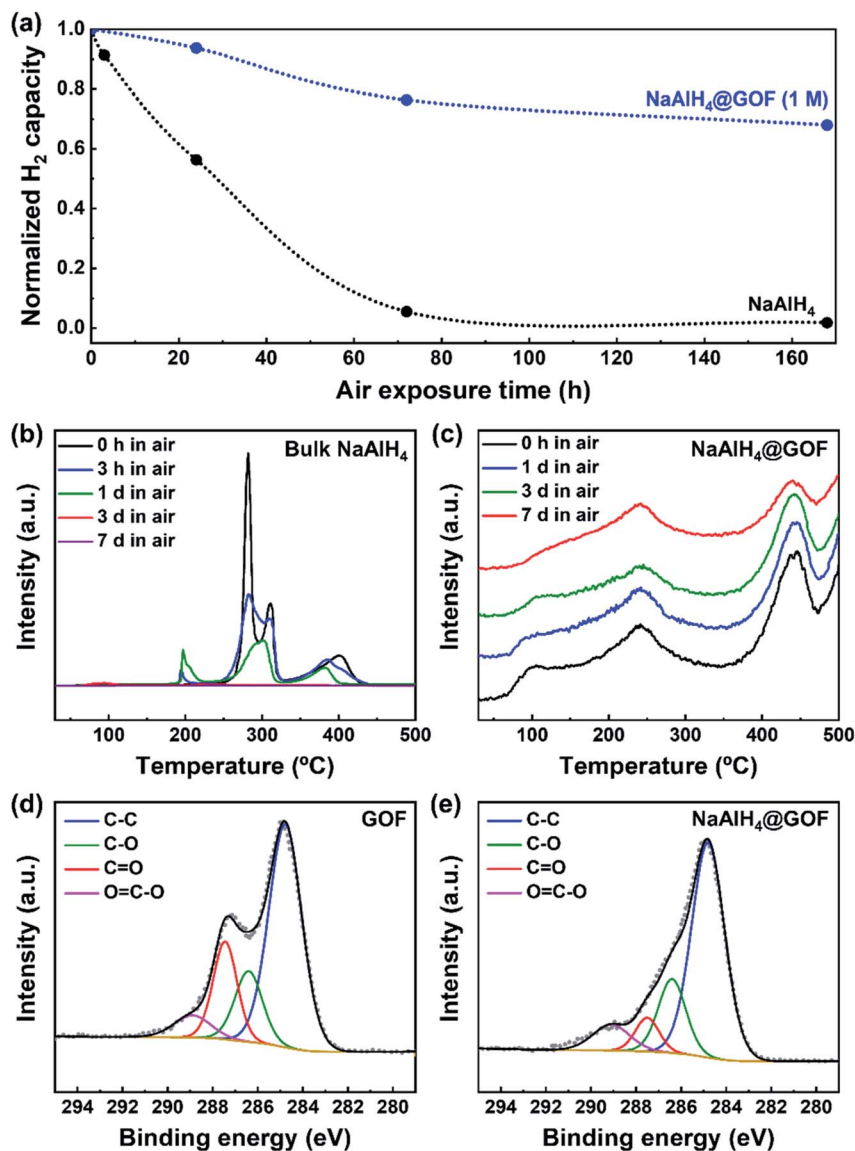
Fig. 4 Hydrogen desorption performance of bulk NaAlH$_4$ and NaAlH$_4$@GOF (1 M) upon air exposure, and XPS spectra of GOF and NaAlH$_4$@GOF (1 M). (a) Normalized hydrogen capacity of bulk NaAlH$_4$ and NaAlH$_4$@GOF exposed to air for 0 h, 3 h, 1 d, 3 d, and 7 d. (b) TPD-MS profiles of air-exposed bulk NaAlH$_4$ at a heating rate of 10.0 °C min^{-1}. (c) TPD-MS profiles of air-exposed NaAlH$_4$@GOF (1 M) at a heating rate of 10.0 °C min^{-1}. (d) C 1s XPS spectra of as-synthesized GOF. (e) C 1s XPS spectra of as-synthesized NaAlH$_4$@GOF (1 M).

The three desorption peaks for bulk NaAlH$_4$, which correspond to the desorption reaction of NaAlH$_4$, Na$_3$AlH$_6$, and NaH, were 282 °C, 311 °C, and 401 °C, respectively, measured at a heating rate of 10.0 °C min^{-1}. Above 400 °C, the dehydrogenation of NaAlH$_4$@GOF occurs at a higher temperature than bulk NaAlH$_4$. The redox reaction between oxygen in the remained THF and NaAlH$_4$ – which likely make Al$_x$O$_y$ nanoclusters-also releases hydrogen, and this is revealed as dehydrogenation at a higher temperature and higher activation energy of dehydrogenation in step 3 (Fig. 3a).[31,32] We focused our investigation on the first two reaction steps, which are of interest for practical applications as these desorption reactions proceed at relatively lower temperatures and are known to be reversible. In the TPD-MS profile of NaAlH$_4$@GOF (1 M) (Fig. 3d), the desorption

temperatures for the first and second reaction step measured at a heating rate of 10.0 °C min^{-1} are significantly reduced to 108 °C and 231 °C, respectively. As some amount of confined NaAlH$_4$ directly reacts with oxygen elements from GOF and THF, leading to the early decomposition of NaAlH$_4$, it diminishes the hydrogen capacity in the first step compared to bulk NaAlH$_4$.[31]

We calculated the activation energy for the hydrogen desorption of both bulk and nanoconfined NaAlH$_4$ using the Kissinger equation,[33] and the results from each step are presented in Fig. 3a. The Kissinger plots corresponding to bulk NaAlH$_4$ and NaAlH$_4$@GOF (1 M) are shown in Fig. 3c and e, respectively. The activation energy of the hydrogen desorption process can be determined according to the following equation:

$$\ln\left(\frac{\beta}{T_p{}^2}\right) = \left(-\frac{E_a}{R}\right)\frac{1}{T_p} + \ln\left(\frac{AR}{E_a}\right)$$

where β is the heating rate, T_p is the peak temperature obtained from the TPD-MS profile, E_a is the activation energy, R is the universal gas constant, and A is a pre-exponential factor. Therefore, activation energy can be estimated from the slope in the Kissinger plot of $\ln\left(\frac{\beta}{T_p{}^2}\right)$ *versus* $\frac{1}{T_p}$. The activation energy for the first and second desorption reaction is 124.30 kJ mol^{-1} and 148.76 kJ mol^{-1} for bulk NaAlH$_4$, agreeing with the prior reports (Table S1†). Upon the confinement inside the nanoporous GOF, the activation energy decreases to 47.13 kJ mol^{-1} for the first reaction and 108.45 kJ mol^{-1} for the second reaction, demonstrating a remarkable improvement in the hydrogen desorption performance. The activation energy values for NaAlH$_4$@GOF are comparable to or even smaller than the previous results in which NaAlH$_4$ samples were doped with transition metal-based catalysts (Table S1†), presumably attributed to the well-defined nanoporous structure of GOF. It can be deduced that NaAlH$_4$ particles are confined within 1–2 nm size of GOF pores – which is confirmed by BET measurements and d-spacing values – and this significantly boosts the nanoconfinement effect, resulting in the substantial kinetic enhancement without using transition metals as catalysts.

Interestingly, in addition to the decrease in the activation energies, we observed a loss in hydrogen capacity for NaAlH$_4$@GOF. For bulk NaAlH$_4$, the amount of hydrogen released was measured to be 6.10 wt% based on the area below the TPD-MS curve. For NaAlH$_4$@GOF (1 M), the amount of hydrogen released was measured to be 1.01 wt% for the infiltrated NaAlH$_4$ inside the composite, assuming 20.0 wt% NaAlH$_4$ loading from ICP-OES results. The measured hydrogen capacity of NaAlH$_4$@GOF corresponds to only 16.6% of that of bulk NaAlH$_4$. We believe that this capacity loss is caused by oxygen functional groups in the GOF, which reacts with NaAlH$_4$ and are reduced during the wetness impregnation process. To verify our hypothesis, we measured Raman spectra of GO and GOF (1 : 4). The Raman spectra (Fig. S6†) of GO and GOF (1 : 4) are nearly identical in position and intensity of the D-band peak around 1340 cm^{-1} and G-band peak around 1580 cm^{-1}, suggesting that functional groups of GO remain in GOF even when a high linker concentration is used for synthesis. This observation agrees with the FT-IR spectra, where a broad O–H stretch is observed for all GOF samples (Fig. 1d). This issue may be addressed in the future by reacting the GOF with hydrogen or reducing oxygen functional groups in the GOF prior to wetness impregnation.[34]

On the other hand, the reduction of oxygen functional groups in the GOF during the wetness impregnation step leads to an improvement in air stability for NaAlH$_4$@GOF. NaAlH$_4$ is extremely reactive towards O$_2$ and H$_2$O, and oxidizes rapidly upon exposure to air.[35] TPD-MS profiles of bulk NaAlH$_4$ and NaAlH$_4$@GOF (1 M) upon different durations of air exposure show a clear enhancement of air stability for the confined sample (Fig. 4a–c). The TPD-MS profile of air-exposed NaAlH$_4$ showed the formation and disappearance of a desorption peak

around 200 °C, which may be caused by destabilization from the reaction product between NaAlH$_4$ and O$_2$, H$_2$O, *etc.* under ambient conditions.[36] After 7 days of air exposure, bulk NaAlH$_4$ retains only 1.8% of its initial hydrogen capacity whereas NaAlH$_4$@GOF maintains 68.0% of its initial hydrogen capacity. To investigate the differences in chemical state of GOF caused by NaAlH$_4$, we measured C 1s XPS spectra of GOF and NaAlH$_4$@GOF (1 M) (Fig. 4d and e). The relative peak area corresponding to the C=O chemical state decreases from 18.75% in GOF to 7.23% in NaAlH$_4$@GOF. We believe that the improved air stability is caused by surface-reduced GOF acting as a barrier layer for H$_2$O and O$_2$, similar to selective gas permeation observed in reduced graphene oxide sheets.[27,37,38]

Conclusions

In summary, this work demonstrates the viability of utilizing GOF as a nanoscaffold for confining hydrogen storage material for the first time. The framework structure with an optimized d-spacing results in a noticeable nanoconfinement effect for NaAlH$_4$ in which both the onset hydrogen desorption temperature and the activation energy for the first two reversible hydrogen desorption reactions of NaAlH$_4$ are significantly reduced without transition metal catalysts.

However, hydrogen capacity loss is observed in the nanocomposite, possibly caused by the detrimental reaction between NaAlH$_4$ and oxygen functional groups in the GOF. At the same time, the air stability of the confined NaAlH$_4$ is dramatically improved as a result of the formation of surface-reduced GOF during NaAlH$_4$ infiltration acting as a barrier layer. Although we focused our study on NaAlH$_4$, the beneficial effect of GOF as a nanoporous host for confinement may be extended to other metal hydrides. Future work will involve optimizing the synthesis process to increase active NaAlH$_4$ content, and studying the possible catalytic effect of boron atoms inside the GOF on the hydrogen storage behaviour of the GOF-based nanocomposites.

Conflicts of interest

There are no conflicts to declare.

Acknowledgements

References

1 A. Sartbaeva, V. L. Kuznetsov, S. A. Wells and P. P. Edwards, *Energy Environ. Sci.*, 2008, **1**, 79–85.

2 A. Schneemann, J. L. White, S. Kang, S. Jeong, L. F. Wan, E. S. Cho, T. W. Heo, D. Prendergast, J. J. Urban, B. C. Wood, M. D. Allendorf and V. Stavila, *Chem. Rev.*, 2018, **118**, 10775–10839.

3 I. P. Jain, P. Jain and A. Jain, *J. Alloys Compd.*, 2010, **503**, 303–339.

4 B. Bogdanović and M. Schwickardi, *J. Alloys Compd.*, 1997, **253–254**, 1–9.

5 C. P. Baldé, H. A. Stil, A. M. J. van der Eerden, K. P. de Jong and J. H. Bitter, *J. Phys. Chem. C*, 2007, **111**, 2797–2802.

6 B. Bogdanović, M. Felderhoff, A. Pommerin, F. Schüth and N. Spielkamp, *Adv. Mater.*, 2006, **18**, 1198–1201.

7 Q. Gao, G. Xia and X. Yu, *Nanoscale*, 2017, **9**, 14612–14619.

8 Z. Yuan, Y. Fan, Y. Chen, X. Liu, B. Liu and S. Han, *Int. J. Hydrogen Energy*, 2020, **45**, 21666–21675.

9 X. Zhang, Y. Liu, K. Wang, Y. Li, M. Gao and H. Pan, *ChemSusChem*, 2015, **8**, 4180–4188.

10 Y. Liu, X. Zhang, K. Wang, Y. Yang, M. Gao and H. Pan, *J. Mater. Chem. A*, 2016, **4**, 1087–1095.

11 P. E. de Jongh and P. Adelhelm, *ChemSusChem*, 2010, **3**, 1332–1348.

12 T. K. Nielsen, F. Besenbacher and T. R. Jensen, *Nanoscale*, 2011, **3**, 2086–2098.

13 Y. Li, G. Zhou, F. Fang, X. Yu, Q. Zhang, L. Ouyang, M. Zhu and D. Sun, *Acta Mater.*, 2011, **59**, 1829–1838.

14 C. L. Carr, W. Jayawardana, H. Zou, J. L. White, F. El Gabaly, M. S. Conradi, V. Stavila, M. D. Allendorf and E. H. Majzoub, *Chem. Mater.*, 2018, **30**, 2930–2938.

15 U. Jeong, H. Kim, S. Ramesh, N. A. Dogan, S. Wongwilawan, S. Kang, J. Park, E. S. Cho and C. T. Yavuz, *Angew. Chem., Int. Ed.*, 2021, **60**, 22478–22486.

16 T. K. Nielsen, M. Polanski, D. Zasada, P. Javadian, F. Besenbacher, J. Bystrzycki, J. Skibsted and T. R. Jensen, *ACS Nano*, 2011, **5**, 4056–4064.

17 C. P. Baldé, B. P. C. Hereijgers, J. H. Bitter and K. P. de Jong, *J. Am. Chem. Soc.*, 2006, **45**, 3501–3503.

18 C. P. Baldé, B. P. C. Hereijgers, J. H. Bitter and K. P. d. Jong, *J. Am. Chem. Soc.*, 2008, **130**, 6761–6765.

19 M. Christian and K.-F. Aguey-Zinsou, *Nanoscale*, 2010, **2**, 2587–2590.

20 S. Zheng, F. Fang, G. Zhou, G. Chen, L. Ouyang, M. Zhu and D. Sun, *Chem. Mater.*, 2008, **20**, 3954–3958.

21 R. K. Bhakta, J. L. Herberg, B. Jacobs, A. Highley, R. Behrens Jr, N. W. Ockwig, J. A. Greathouse and M. D. Allendorf, *J. Am. Chem. Soc.*, 2009, **131**, 13198–13199.

22 V. Stavila, R. K. Bhakta, T. M. Alam, E. H. Majzoub and M. D. Allendorf, *ACS Nano*, 2012, **6**, 9807–9817.

23 E. Ianni, M. V. Sofianos, M. R. Rowles, D. A. Sheppard, T. D. Humphries and C. E. Buckley, *Int. J. Hydrogen Energy*, 2018, **43**, 17309–17317.

24 J. W. Burress, S. Gadipelli, J. Ford, J. M. Simmons, W. Zhou and T. Yildirim, *Angew. Chem., Int. Ed.*, 2010, **49**, 8902–8904.

25 Y. Zhang, S. Zhang and T.-S. Chung, *Environ. Sci. Technol.*, 2015, **49**, 10235–10242.

26 S. Kim, J. Choi, C. Choi, J. Heo, D. W. Kim, J. Y. Lee, Y. T. Hong, H.-T. Jung and H.-T. Kim, *Nano Lett.*, 2018, **18**, 3962–3968.

27 E. S. Cho, A. M. Ruminski, S. Aloni, Y.-S. Liu, J. Guo and J. J. Urban, *Nat. Commun.*, 2016, **7**, 10804.

28 K. Severin, *Dalton Trans.*, 2009, **27**, 5254–5264.

29 G. Srinivas, J. W. Burress, J. Ford and T. Yildirim, *J. Mater. Chem.*, 2011, **21**, 11323–11329.

30 S. Gomes, G. Renaudin, H. Hagemann, K. Yvon, M. P. Sulic and C. M. Jensen, *J. Alloys Compd.*, 2005, **390**, 305–313.

31 S. Chumphongphan, U. Filsø, M. Paskevicius, D. A. Sheppard, T. R. Jensen and C. E. Buckley, *Int. J. Hydrogen Energy*, 2014, **39**, 11103–11109.

32 E. H. Majzoub, J. L. Herberg, R. Stumpf, S. Spangler and R. S. Maxwell, *J. Alloys Compd.*, 2005, **394**, 265–270.

33 H. E. Kissinger, *Anal. Chem.*, 1957, **29**, 1702–1706.

34 S. Pei and H.-M. Cheng, *Carbon*, 2012, **50**, 3210–3228.

35 M. H. W. Verkuijlen, R. de Gelder, P. J. M. van Bentum and A. P. M. Kentgens, *J. Phys. Chem. C*, 2011, **115**, 7002–7011.

36 D. E. Dedrick, R. Behrens and R. J. S. N. L. Bradshaw, *Sandia Report*, 2007, 4960, pp. 1–57.

37 E. S. Cho, A. M. Ruminski, Y.-S. Liu, P. T. Shea, S. Kang, E. W. Zaia, J. Y. Park, Y.-D. Chuang, J. M. Yuk, X. Zhou, T. W. Heo, J. Guo, B. C. Wood and J. J. Urban, *Adv. Funct. Mater.*, 2017, **27**, 1704316.

38 D. J. Han, S. Kim and E. S. Cho, *J. Mater. Chem. A*, 2021, **9**, 9875–9881.